

# Benefits of Rotating Rig Facility for the Study of Droplet Deformation and Breakup in the Vicinity of Aerodynamic Surfaces

*Adelaida Garcia-Magariño\*, Suthyvann Sor\*\*, Rafael Bardera\*\*\* and Juan Palacios\*\*\**

*Instituto Nacional de Tecnica Aeroespacial*

*Carretera de Ajalvir km 4, 28850, Torrejon de Ardoz,*

*\*garciamga@inta.es, \*\* sors@inta.es, \*\*\*barderar@inta.es, \*\*\*\* palaciosj@inta.es*

## Abstract

During in-flight conditions, aircraft may encounter clouds containing supercooled large droplets (SLD) thus creating ice depending on the droplets impact location and the size of the droplets. The aim of this work is to show the benefits of the rotating rig facility as compared to wind tunnel facility to study droplet deformation and breakup phenomenon in the vicinity of the leading edge of airfoils. The cost of operation of this installation is considerably lower and higher velocities (up to 90 m/s) can be obtained, at the same time that the generation of the droplets is also easier.

## 1. Introduction

During in-flight conditions, aircraft may encounter clouds containing supercooled large droplets (SLD) that may impact on wing surfaces thus creating ice [1, 2]. Heavy rain conditions can also degrade the aircraft performances depending on the droplets impact location and the size of the droplets [3, 4]. The droplets contained in the cloud would suffer a continuously accelerated flow field when they are approached by the wing surfaces [5]. Droplet deforms as an oblate spheroid due to the airflow and under certain conditions droplets may even breakup before impinging thus changing the droplet size, and the impact location [6, 7]. Droplet deformation and breakup due to airstreams have been studied along the last middle century. However, experimental data of breakup was obtained in shock tubes installations where droplets are suddenly exposed to a constant high-speed stream [8, 9, 10]. Though this information was at first included for developing models in the simulation codes that describes the phenomenon of SLD and heavy rain [11], this is not the same flow field that droplets would encounter in the real situation (continuously accelerated flow field). Moreover, there exists studies on droplets that confirms that droplet behaviour subjected to acceleration flow field differs from those subjected to deceleration [12]. In this context, the rotating rig facility at INTA was built [13] and several improvements have been made up to the current configuration. The aim of this work is to show the benefits of the rotating rig facility as compared to wind tunnel facility to study droplet deformation and breakup phenomenon in the vicinity of the leading edge of airfoils. First the experimental facility is described and discussed, and the characterization of the flow field generated by the new set of airfoils models is presented. Secondly, the influence of airfoil wake in the test section and the two-dimensionality assumption are evaluated. Then the comparison between the rotating arm facility versus the wind tunnel facility is presented. Finally, as a proof of the benefits of the rotating arm facility, the main droplet deformation and breakup models developed in the facility are shown and future application in the facility are studied.

## 2. General Description of the Rotating Rig Facility

The rotating arm unit consists of a motor inside a supply support that rotates a moving arm of 2 m at which end there is an airfoil model. In droplet deformation and breakup tests, droplets are allowed to fall in the path of the incoming airfoil. A photograph of the Rotating Rig facility is shown in Figure 1. Each part of the unit, the droplet generation and the data acquisition system are described in the following sections. The experiments were done in a square room of 6.5 m side and 3.65 m height. Moreover, a new safety measure has been added: a metallic grid of squares of 3.5 cm x 3.5 cm and 3 cm depth between the operation room and the test section.



Figure 1: Rotating Rig Facility

## 2.1 Motor and Supply Structure

A 5.0 KW DC Electric Motor with forced ventilation and a temperature sensor to disconnect the electric supply in case of overheating is housed inside the supply structure. The supply structure is made of hollow steel beams and is welded to a steel plate attached to a concrete block on the floor. This allows to support the stresses generated to move the rotating arm at velocities up to 90 m/s. The structure form and its dimensions are shown in Figure 2. A new Varmec RCV 381 gearbox has been added between the motor and the transmission gears to take advantage of all the power of the motor for certain models. Then, the vertical axle is connected to the arm's head (see Figure 2). In the supply structure is also placed the electronic control system and 12 channels slip rings

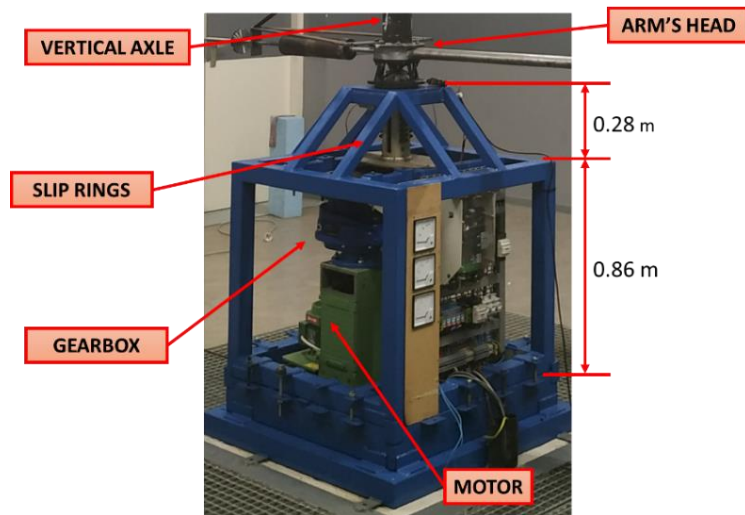


Figure 2: The supply structure photograph

## 2.3 Droplet Generation

Droplet are generated using the Rayleigh theory that established that if a jet of a certain diameter  $d_j$  is vibrated near the Rayleigh frequency  $f_R$  (wavelength equals to 4.5 jet diameter), the jet will breakup into a monodisperse stream of droplets of diameter  $d$ . The droplet diameter is related to the flow rate  $Q$  and the frequency  $f$  by the following relation:

$$d = \sqrt[3]{\frac{6Q}{\pi f}} \quad (1)$$

Two monosized droplet generators are available: a TSI MDG-100 and the in-house monodisperse droplet generator shown in Figure 3. The first one allows the obtention of droplets diameters from 300 to 1500  $\mu\text{m}$ , while the second one allows bigger droplets up to 3600  $\mu\text{m}$ . The sketch of the in-house monodisperse generator and the calibration of the flow rate is shown also in Figure 3.

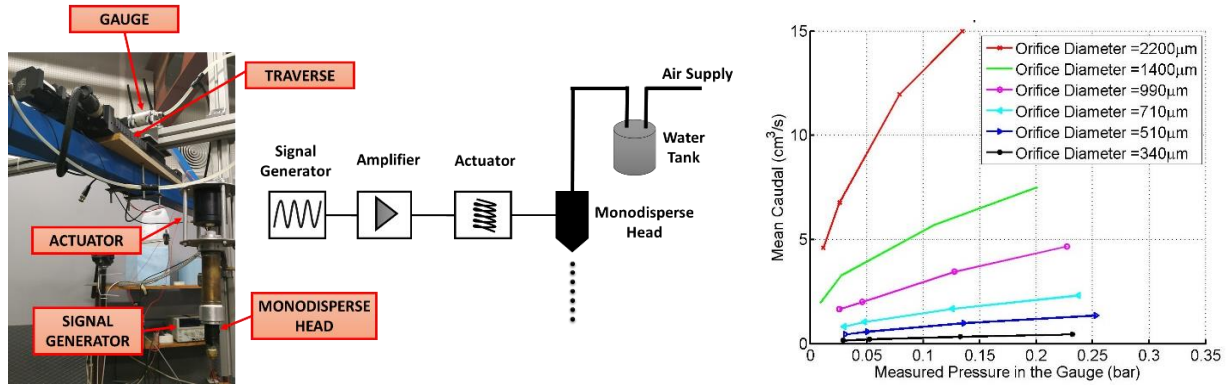


Figure 3: Droplet generator photograph (on the left), sketch (on the center), and flow rate calibration (on the right).

### 2.3 Airfoil Model

The airfoil model is mounted at the end of the rotating arm and is responsible for the air velocity increase in the test section (where droplets fall). The airfoil models are usually built out of Styrofoam in order to reduce the weight of them. They are symmetric respect to the plane of rotation of the arm in order to avoid lift forces into the arm. They usually consist of a central part, which is two dimensional and whose profile depends on the specific model, and two lateral axisymmetric parts of the same profile (See Figure 4 on the left). The profiles of the model used in the facility are plotted in Figure 4 on the right. Table 1 shows a summary of the models available in the facility, including the five recent new models (DBK004, P0, P1, P4 and C1).

Table 1: Airfoils Models

MODEL	Profile	Chord (mm)	Span (mm)	Thickness (mm)	Leading Edge Radius (mm)	Cd
DBK001	DBK	200	200	40	15	0.00938
DBK002	DBK	470	200	95	35	0.00938
DBK003	DBK	690	200	139	51	0.00938
DBK004	DBK	1050	300	211	78	0.00938
P0	P0	640	500	129	297	-
P1	P1	650	500	130	173	0.01084
P4	P4	770	450	155	34	0.00891
C1	C1	660	500	132	18	0.01157

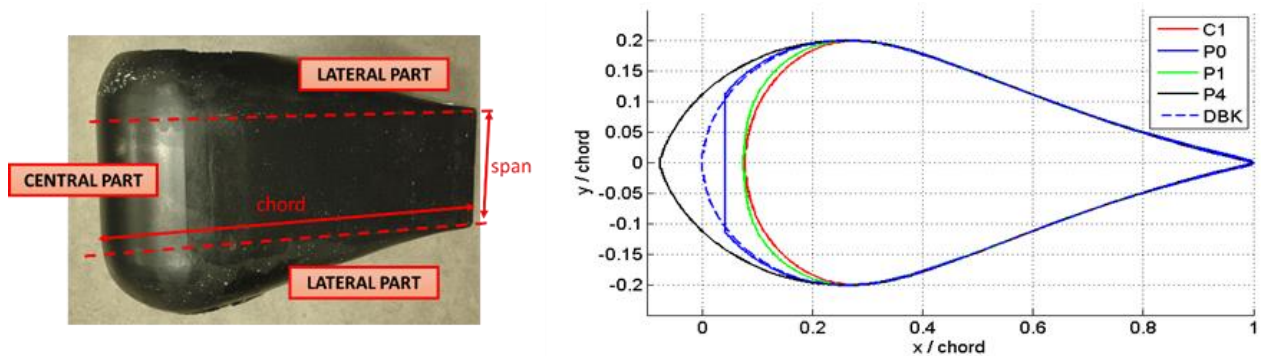


Figure 4: Airfoils models

## 2.4 Data Acquisition System

The type of acquisition system depends of the type of camera used, either a high resolution camera or a high speed camera, and the type of the illumination, either direct illumination or shadowgraph illumination. The high resolution camera allows obtaining a higher resolution, however, in order to capture droplets at a specific instant a pulse illumination system is required. In contraposition, the high-speed camera does not need of a pulse illumination and allow the tracking of the same droplet. Shadowgraph illumination is needed to quantify the deformation, while direct illumination allows a better comprehension of the whole phenomenon. The sensibility of the camera needs to be higher since the illumination last very short times, on the order of microseconds. The color information is not usually needed and therefore it could be selected a black and white camera in order to have more sensibility. The main high-resolution cameras used in the installation have been the NIKKON DE800E (resolution of 36.3 Megapixels and a sensibility ISO up to 6400) and the Hasselblad H3DII-39 (resolution of 39 Megapixels and sensitivity ISO up to 800). The high speed camera used have been the PHOTRON SA-5 (acquisition rate from 7500 to  $10^6$  fps and ISO up to  $10^4$ ) and the PHOTRON SA 4 (acquisition rate from 3600 to  $0.5 \cdot 10^6$  fps and ISO up to 6400). A compromise between the acquisition rate and the resolution needs to be found. For the high speed camera, the source of light needs to have a great intensity, and therefore it is usually used the xenon lamps or more recently the LED lamps. As flash illumination three types are available: a microflash (General Radio 1538-A strobotac,  $4\mu\text{s}$  of flash duration), a nanoflash (High-speed-photo-system, NANOLITER, 20 ns of flash duration) and a Nd-Yag laser (TSI, Surelite, 8 ns of flash duration).

## 3. Characterization of the flow field of the new models

In order to characterize the flow field generated by the new models, laser doppler velocimetry (LDV) measurements in the test section (along the stagnation line of the pass of the model) have been performed. The measurements near the leading edge of the model are used in this section to characterise the air velocity that the droplet would, while the measurements in the wake of the airfoil will be used in the next section.

### 3.1 Description of the experiments

The four new models P0, P1, C1 and P4 described in previous sections will be tested for model velocities of 30 m/s and 60 m/s. The experimental matrix tested is summarized in the following Table 2.

Table 2: Experimental Matrix

	<b>Model P0</b>	<b>Model P1</b>	<b>Model C1</b>	<b>Model P4</b>
$U_m = 30$ m/s	Case #1	Case #3	Case #5	Case #7
$U_m = 60$ m/s	Case #2	Case #4	Case #6	Case #8

In order to measure the velocity with LDV technique, the particle seeding system used was a Laskin oil droplet atomizer placed near the LDV laser probe where the laser and all the optical set up of the LDV system are housed. The probe was fixed at 45 cm of height from the measurement point, which was located at the midpoint of the span of the airfoil and contained in the plane of the stagnation line of the airfoil. A photograph experimental setup is seen in Figure 5. The orientation of the probe was placed to measure the velocity component perpendicular to the leading edge at the stagnation line in the plane mentioned before. The experiments were done with DANTEC LDV system composed of three different elements: a FlowLite integrated laser-optics unit, a BSA-F60 Flow Processor and the BSA Flow Software. This system used two laser beams of 632.8 nm of wavelength (red light) with 40MHz of optical shift between them, and it generates an ellipsoid measurement volume of 26  $\mu\text{m}$  length, 2.13  $\mu\text{m}$  width, and 2.14  $\mu\text{m}$  width. For data acquisition at 30m/s, a velocity centering of 18.77m/s combined with a velocity span of 25.05m/s was used, whereas for experiments at 60 m/s the velocity centering and the velocity span used were 37.58m/s and 50.10m/s respectively.

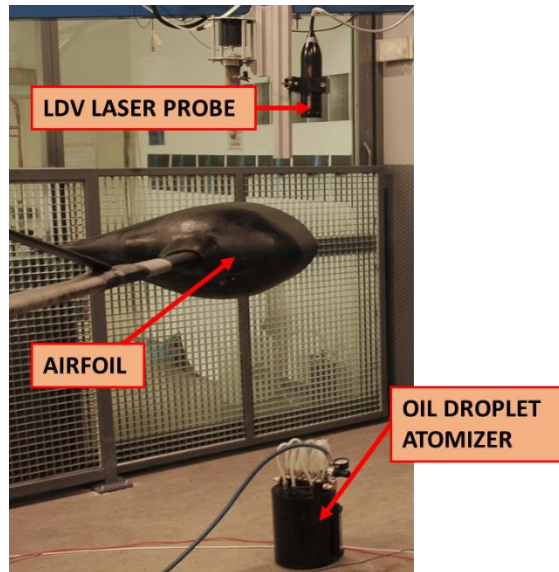


Figure 5: LDV experimental Setup

### 3.2 Data Analysis

Due to the rotation of the profile, the acquired data has a pattern behaviour with repetition cycles of approximately 131rpm and 262rpm, which are the rotational speeds of the rig facility at 30m/s and 60m/s experiments, respectively. Using that feature, the moment in which the trailing edge passes through the measurement point in each cycle can be calculated. To do so, the trailing edge pass is assumed to occur at the maximum value of the velocity measured from half of the previous cycle to half of the estimated duration of the new cycle, if and only if, that value is greater than the 95% of the estimated model velocity of the new cycle. The duration and velocity of the new cycle are assumed to be equal to the duration and the velocity of the previous one. Once the position of the trailing edge is known, all the cycles are superposed, and the data value that determine each pass is filtered and plots like the ones shown in Figure 7 and 8. Finally, equation 2 is used to fit all the data up to distances to the leading edge of 1.5 times the chord. In that equation, the constants  $a_1$ ,  $a_2$  and  $a_3$  represents the fitting parameters.

$$U/U_m = a_1 e^{a_2} + a_3 \quad (2)$$

With regards to the errors, there are two main sources of them: the first one, associated to the trailing edge detection; and the second one, associated to the error made in the chord measurements. As can be seen in Figure 7 and Figure 8, the data dispersion close to the leading edge is small. Therefore, the trailing edge detection error is considered negligible. However, the dimensionless velocity in Figure 6 (right) does not reach 1 at the theoretical leading-edge position (which would be due to the error in the chord measurement). A shift is done in resultant curve from equation 2 to correct it.

### 3.3 Experimental results

In Figure 6 on the left is shown an example of how the fitting curve is adjusted to the experimental data obtained. Doing the fitting for the experimental data of the four models and plotting the results in dimensionless air velocity profile versus the distance to the leading edge of the model divided by the chord, Figure 6 on the right is obtained. The DBK model profile is also added in that figure to compare it with the results obtained for the new airfoil models. It can be observed that as the leading-edge curvature increases (in increasing order P0, P1, C1, DBK and P4), the velocity profile becomes more abrupt.

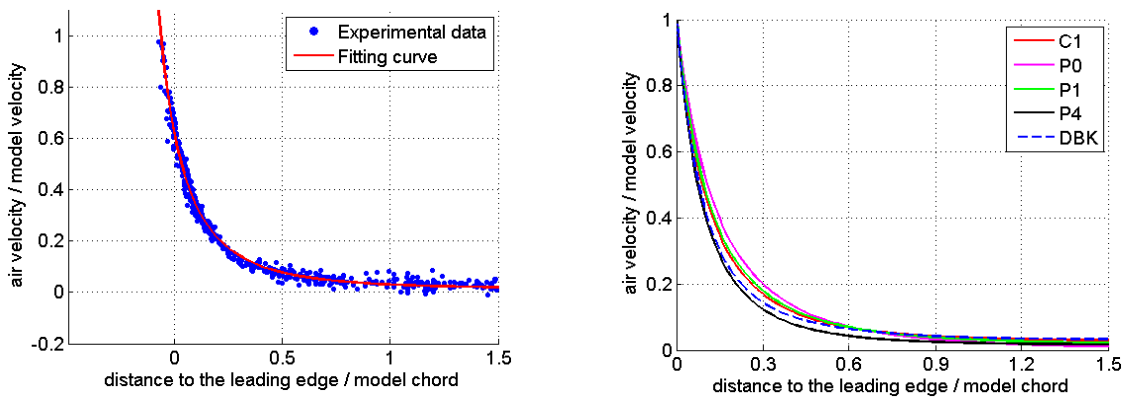


Figure 6: Fitting of the LDV measurements of P1 (on the left) and comparison of velocity profiles (on the right)

#### 4. Experimental study of the influence of the wake in the test section

The measurements of the experiments described in previous section also led to the obtention of air velocity measurements all along from the pass of the model to the next pass of the model thus providing measurements of the air velocity of the wake of airfoil model. Data air velocity measurements divided by the model velocity are represented versus the distance to the trailing edge of the model divided by the chord for all the model tested (P0, P1, C1 and P4) in Figures 7 and 8.

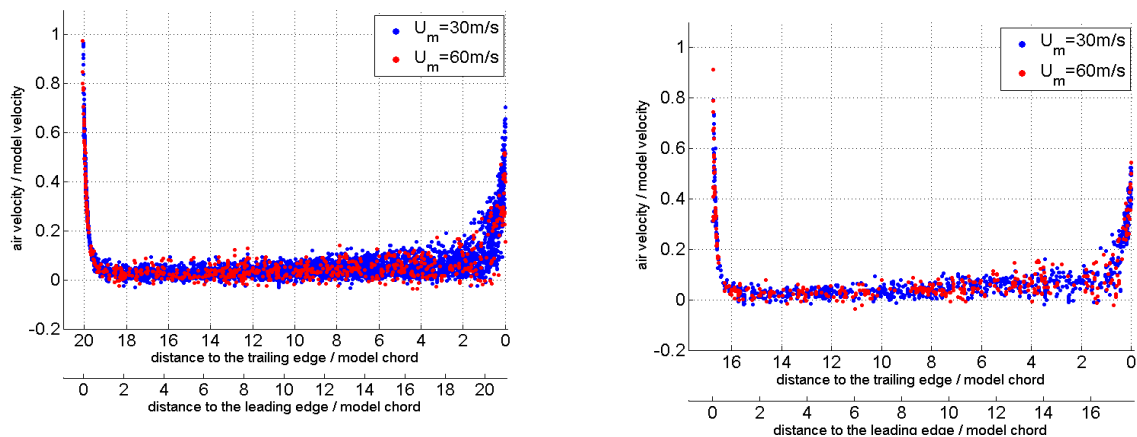


Figure 7: LDV wake measurements for model P1 (on the left) and model P4 (on the right)

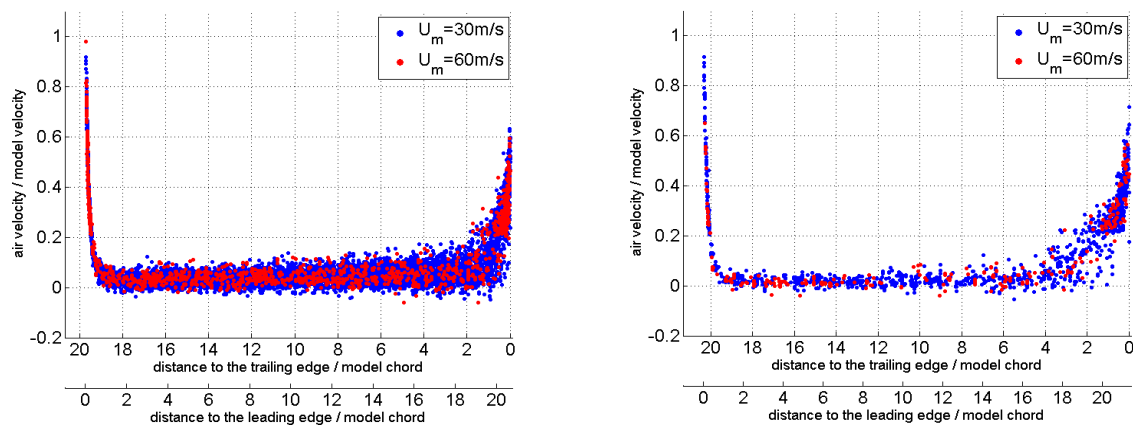


Figure 8: LDV wake measurements for model C1 (on the left) and model P0 (on the right).

The wake of model P1 is observed in Figure 7 on the left. Blue points correspond to model velocity during the test of 30 m/s while red points correspond to 60 m/s test. The Reynolds number for each velocity was  $1.5 \cdot 10^6$  and  $3 \cdot 10^6$  respectively. No influence of the Reynolds number in the velocities in the wake is observed for the range of Reynolds number tested. The velocities inside the wake are reduced to 17% of the model velocity at a distance of three chords to the trailing edge. Then the wake seems to reduce linearly with the distance to the trailing-edge divided by the chord being the slope 0.7%. Finally, when the next pass of the model starts to influence the air in the test section, at a distance to the leading-edge of the model of one chord, the residual velocity of the wake is 3.3% of the model velocity. As the model approaches more the measurement point, the influence of the wake is less noticed becoming negligible very near the leading-edge model. The wake of model P4 is shown in Figure 7 on the right, while the wakes of model C1 model and P4 model are shown in Figure 8. Similar behavior is observed for the others models being the residual velocity at one chord on the order of 2.2%, 3.8% and 2.6% for the model P4, C1 and P0 respectively. Therefore, it can be concluded that the effect of the wake in the test section is a residual velocity that ranges from 2% to 4% in the worst scenario at one chord to the leading-edge of the model. However, as the model approaches, the influence becomes negligible.

## 5. Experimental study of the two-dimensionality in the test section

An experimental campaign has been conducted to evaluate the assumption of two-dimensionality in the test section. The experimental setup is shown in Figure 9. Particle Image Velocimetry (PIV) system has been used to this end. The PIV system consisted of two Neodymium-YAG lasers of 190 mJ/pulse with a pulse duration of 8ns, a synchronizer Model 610035 with resolution 1 ns, a PowerView Plus 4MP camera, a Laskin atomizer of oil particles of  $1 \mu\text{m}$  and the INSIGHT 3G program to cross-correlate the pair of images. The camera, that has a resolution of  $2048 \times 2048$  pixels, 12 bits of intensity dynamic range and a pixel size of  $7.4 \mu\text{m}$ , was located above the test section. The camera lens focal length was 50 mm and the aperture was  $f\#1/5.6$ . The laser lens was a cylindrical lens of focal length -25 mm or -15 mm and spherical lens of focal length of 2000 mm or 1000 mm. The field of view size was on the order of  $200 \times 200 \text{ mm}^2$ , leading to a resolution of  $98 \mu\text{m}/\text{pix}$ . The spot size was on the order of 6 mm. Two model sizes (model DBK002 and model DBK003) and two model velocities (66m/s and 90 m/s) were used in this investigation.

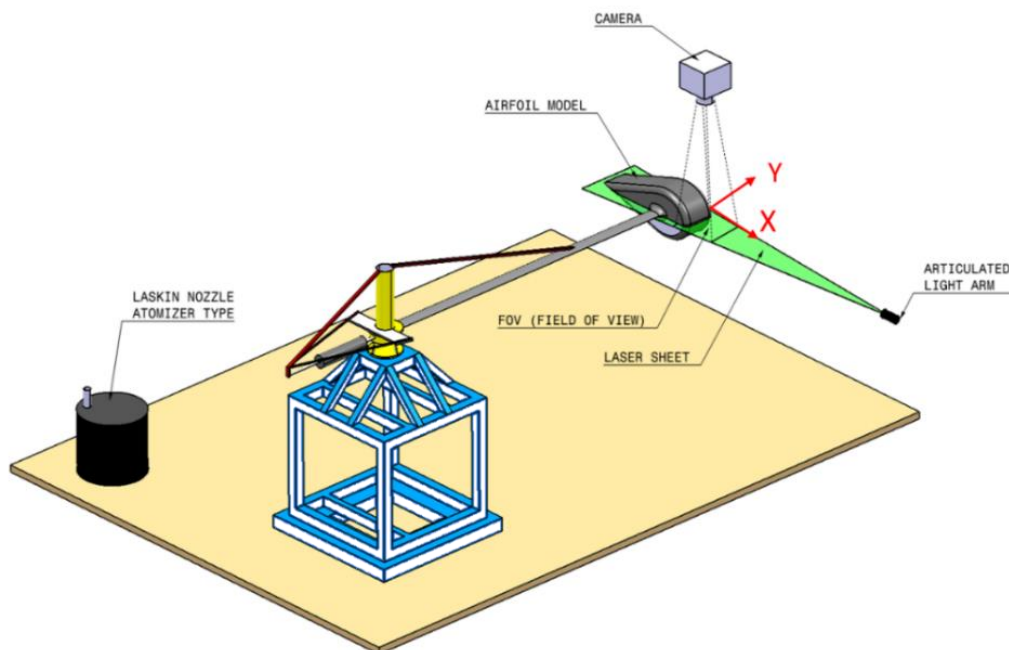


Figure 9: Experimental setup for the PIV tests of the horizontal field of view.

Figure 10 shows the lateral velocity map for the model DBK002 at velocities of 66 m/s (on the left) and 90 m/s (on the right). The axis are the PIV axes, which are plotted in Figure 9. First, it can be observed the similarity between both figures when the maximum lateral velocity is in both cases 7.5% of the model velocity. Then, it can be observed in the figure, that there is a central region in the span-wise direction where two-dimensional can be assumed. Assuming this central region is of width 2 cm, the lateral velocity component would be less than 2% of the velocity magnitude.

Finally, it can be observed a slightly asymmetry that must be due to the fact the model is rotating. However, this asymmetry does not affect the central region where the test section is located.

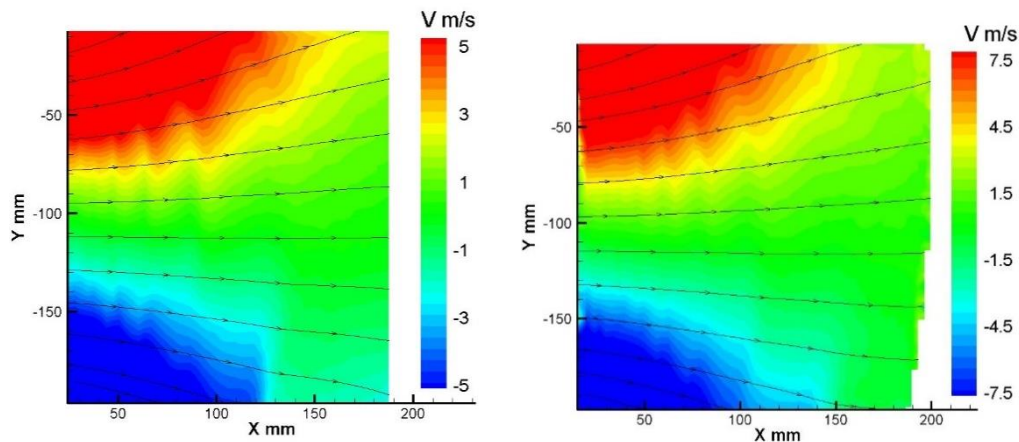


Figure 10: Lateral velocity (in the direction of axis Y in Figure 9) for the model DBK002 moving at 66 m/s (on the left) and 90 m/s (on the right)

## 6. Comparison of the Rotating Rig vs Wind Tunnel

A comparison between the rotating rig facility and the wind tunnel facility is conducted in terms of the evolution of the relative velocity flow field seen by the droplet, the cost of operation, the droplets placement difficulty and the field of view necessary.

### 6.1 Velocity Flow Field

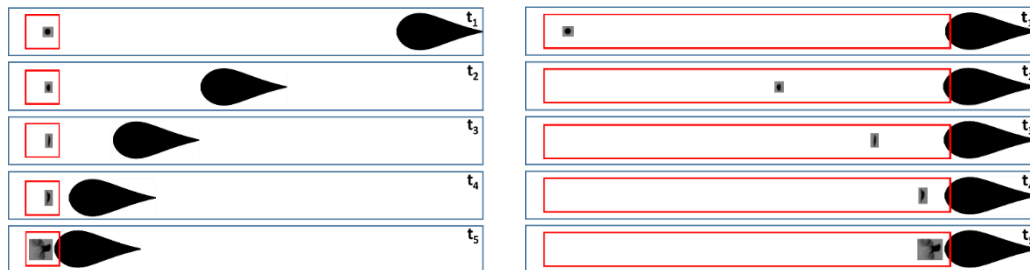


Figure 11: Rotating rig installation concept (left) and wind tunnel installation concept. The red square is the field of view

The conceptual approach of the rotating arm facility and the wind tunnel are shown in Figure 11 right and left respectively. As observed in Figure 11 left, in the rotating rig facility, the droplets fall in the vertical direction while the airfoil is the one that moves at the desired velocity towards the droplets. Due to the movement of the airfoil, the air in front of the leading edge of the airfoil is moved thus creating a flow field velocity that depends on the airfoil shape and the velocity of the airfoil. In the wind tunnel facility, the airfoil model is fixed and the air far from the model is moving at a constant velocity (the freestream velocity). When the air approaches the airfoil model, the air velocity decreases because of the presence of the model. In the end, the relative velocity of the air and the model is the same in both installations at any specific location respect to the airfoil model. Therefore, if droplets initially were moving at the freestream velocity, they would see the same absolute value of the relative velocity respect to the air. However, in the case of the wind tunnel, droplets would decelerate instead of accelerating. And there are some studies that shows differences in the behaviour of droplets in non-stationary flows when they are subjected to acceleration or deceleration [12]. On the other hand, in the rotating arm facility, there exists a residual velocity due to the wake of the previous pass

of the model, and due to the rotation of the model, the two-dimensionality can only be assumed in the very central span-wise region of the model, as discussed in the previous sections.

### 6.1 Operation Cost

The operation cost will be discussed in terms of the power consumption during the tests. In the wind tunnel, the amount of air that has to be moved is considerable higher than the total amount of air moved in the rotating air facility, which leads to a greater consumption. In terms of power, the power consumption of the wind tunnel facility ( $P_{wind\ tunnel}$ ) and rotating arm ( $P_{arm\ rotating}$ ) can be expressed as follows:

$$P_{arm\ rotating} = \frac{1}{2}\rho U_m^3 C_D A_{model} ; P_{wind\ tunnel} = \frac{1}{2}\rho U_{tunnel}^3 S_{tunnel} \quad (3)$$

where  $U_{tunnel}$  is the wind tunnel freestream velocity, which would be considered the same as the model velocity  $U_m$  for comparison purposes. In the equation (3),  $\rho$  stands for air density,  $U_m$  stands for air velocity,  $A_{model}$  stands for the frontal area of the airfoil model,  $S_{tunnel}$  is the area of the test cross section of the wind tunnel and  $C_D$  is the airfoil model drag coefficient. In order to avoid blockage effects in the wind tunnel, the ratio between the frontal area of the model and the area of the cross section should be less than 0.1 [14]. On the other hand, the drag coefficient of the airfoil models tested are on the order of 0.01. Therefore, the power consumption in the rotating rig facility is on the order of 1000 times less than the power consumption of the wind tunnel for the airfoil models available in the rotating arm facility.

### 6.2 Field of view

The field of view necessary to record all the droplets trajectory is shown as red frames for each time in Figure 11 and 12 for rotating rig facility and wind tunnel facility respectively. As observed, the field of view necessary in the wind tunnel facility is considerable larger than the field of view necessary in the rotating rig facility. Usually, the recording starts when droplets are at one chord of the leading edge of the model. For a model chord on the order of 700 mm, the field of view width should be on the order of 700 mm for wind tunnel, while the typical field of view in the rotating arm is on the order of 20 mm. This means that the field of view in the wind tunnel facility should be 35 times the field of view in the rotating rig. This poses a problem for high-speed camera acquisition where the acquisition rate decreases if the field of view increases. Also, it has to be considered that a minimum resolution is needed in order to study the droplet evolution phenomenon taken into account the droplet size, from microns to few millimetres. The camera limitations may prevent the use of the wind tunnel facility for certain droplet deformation application, taken into account the restrictions imposed due to the field of view requirements.

### 6.3 Droplet Placement

In the rotating rig facility, the droplet generation and placement are really easy: droplets are generated and allowed to fall in the path of the incoming airfoil. However, in wind tunnel testing it is one of the most difficult tasks in droplet deformation and breakup studies in the vicinity of airfoils. While in the rotating rig, droplets are initially at calm (except for the falling), in the wind-tunnel droplets should be at the freestream velocity without having been deformed or broken up by the acceleration. Therefore, the acceleration should have been slow enough so as the slip velocity between droplet and the air never exceeded the critical value for the breakup or high deformation. In the end, the acceleration section should be large enough to allow the droplet placement of the droplet without large deformations.

## 7. Principal achievements up to now.

As a result of the experiments conducted in this facility, some new models of droplets deformation, trajectory and breakup have been developed taking into account the continuously accelerated flow field, thus showing the differences to the previous models. The most remarkable achievement up to now are the droplet deformation and trajectory model developed by Sor et al [15] and the droplet breakup criterion for droplets in the vicinity of aircrafts developed by Garcia-Magariño [7]. In the following subsections a brief description of each of them is summarized and some comparison with previous models are presented. These achievements show the adequation of the Rotating Rig facility for the study of these phenomena.

## 7.1 Droplet deformation and trajectory model

The droplet deformation model developed by Sor et al [16] departed from the assumption of an oblate spheroid deformation, the analogy between half of the droplet and a spring-mass system and pure extensional flow. The model is formulated in terms of the motion of the centre of mass of half droplet and the forces acting through the centre of mass. The final expression for the deformation model, expressed in terms of maximum diameter  $D_{max}$ , follows:

$$\frac{1}{64}\pi D^3 \rho_d \frac{d^2 D_{max}}{dt^2} = -\frac{64}{9}\mu_d \pi D^3 \frac{1}{D_{max}^2} \left(\frac{dD_{max}}{dt}\right) - \frac{8}{3}\sigma \frac{dA_s}{dD_{max}} + 0.11\rho_a V_s^2 \pi D^2 \quad (4)$$

where  $D$  is the droplet initial spherical diameter,  $\rho_d$  is the droplet density,  $\mu_d$  is the droplet viscosity,  $\sigma$  is the surface tension of the droplet,  $\rho_a$  is the air density,  $V_s$  is the slip velocity between the air and the droplet.

In order to show the goodness of the model for a droplet that are subjected to an increasingly accelerated flow field, this model is compared to the previous models of DDB developed by Ibrahim et al [17] and the Clarks Model [18]. Figure 12 shows the comparison for a droplet of 930  $\mu\text{m}$  of initial diameter subjected to the flow field generated by the model DBK003 moving at 80 m/s. It is apparent the improvement of the model of Sor et al [15] versus the previous models.

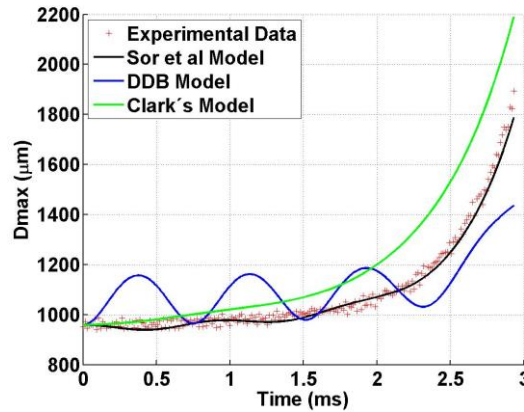


Figure 12: Rotating Rig Facility

A trajectory model including the previous deformation model was also developed by Sor et al [14] where the drag coefficient for the droplet included the non-stationary intrinsic to the problem. In fact, the drag coefficient was modelled by the sum of a stationary terms that takes into account the droplet shape (the degree of deformation) and a non-stationary term that takes into account the acceleration at each time of the slip velocity that the droplet sees. This model was validated thanks to the rotating arm showing that the error was on the order of 3% both for droplets in the stagnation line [15] and for droplets in the shoulder region [19,20] of airfoils.

## 7.2 Breakup criterion

Also, a semi-empirical breakup criterion for droplets in the vicinity of airfoils was developed by Garcia-Magariño et al [7] thanks to the Rotating Rig installation. Though there exists various criteria of droplet breakup for droplet suddenly exposed to a high constant airstream ([21], [8]), this is the only one criterion for droplets subjected to a continuously increasing flow field. A relation is provided by this criterion: the Weber number at which the breakup starts versus the relation of the characteristic time and the flow field variation time:

$$We = 17.5 + 17.9 \frac{t_{def}}{t_{ff}} \quad (5)$$

The characteristic deformation time is defined as the square of the ratio of the half droplet mass and the surface tension, according to the analogy of half droplet and a spring mass-system. In this analogy, the surface tension would be

analogous to the spring force, while the viscous force is analogous to the damping force, and the pressure forces to the external force.

## 8. Preliminary Study of Future Applications

In the near future, some other applications such as studying the droplet deformation and breakup in the splashing phenomenon or testing droplets indeed supercooled will be performed. The main challenges in these other applications and the proof of research already performed will be described in the next sections.

### 8.1 Splashing

In order to study the splashing phenomenon, the main problem is that droplets that depart from the surface moves at higher velocities and they are very small compared to the initial droplet. Therefore, a high-resolution camera and a pulsed illumination is needed. A preliminary proof of research was conducted for different illumination techniques. First of all, direct illumination technique using the micro-flash was employed for droplets of 1mm of diameter falling while the model DBK002 is approaching at velocities from 26 m/s up to 90 m/s. Droplets were generated using the TSI-100 monodisperse droplet generator using an orifice diameter of 700  $\mu\text{m}$  and a frequency of 4.46KHz while the flow rate was 2.33  $\text{cm}^3/\text{s}$ . The camera used was the Hasselblad H3DII-39 with an ISO of 400 and diaphragm aperture of  $f\#1/6.8$ . The camera has a resolution of 7216 pixels (width) x 5412 pixels (height) and the field of view was centred either at 6 mm or at 13 mm above the stagnation line of the model. An example of the images obtained when the airfoil model was moving at 90 m/s and the field of view was centred at 13 mm above the stagnation line is shown in Figure 13. It can be observed that droplet deformation may affect the splashing phenomenon. It can be also observed that the droplets that departs from the surface are blurred, which means that the duration of the microflash is not short enough to capture them.



Figure 13: Droplets of 1 mm splashing on the moving airfoil DBK002 at 90 m/s.

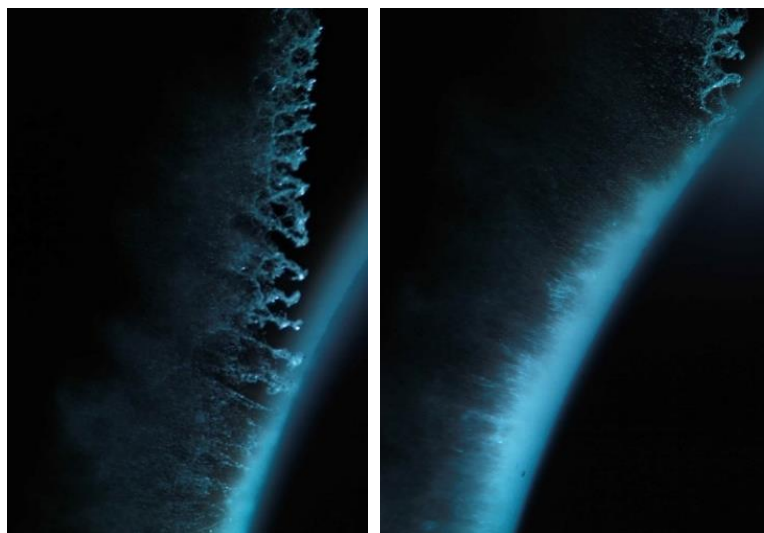


Figure 14: Droplets of 1 mm splashing on the moving airfoil DBK002 at 90 m/s.

Two images obtained for the field of view centred at 6 mm above the stagnation line are presented in Figure 14. The image on the left was taken before than the image on the right. It can be observed that the airfoil model would start impinging the droplets at a location nearer to the stagnation line. It is again shown the influence of droplet breakup in the splashing. It can also be distinguished droplets resultant from droplet breakup (image on the left), which are sharp, from the resultant droplet of the splashing, which are blurred.

Shadowgraph images were also taken with the micro-flash illuminating a screen from the back. The same camera Hasselblad H-DII-39 with a final focal length of 360mm and ISO-200 was used. An example of these images is shown in Figure 15, where the airfoil model was moving at 80 m/s. It can be observed in the Figure 15 that again the resultant droplet of the splashing is blurred because their velocities are higher.



Figure 15: Example of the image taken by shadowgraph technique with the micro-flash and model velocity 80 m/s.

In order to capture the resultant droplets to measure their size, illumination sources whose duration are on the order of nanoseconds were employed. First a laser pulse of duration of 8ns was used to illuminate from the back using a parabolic mirror of focal length of 2 m. The camera used was the Nikon DE800E with a lens of 300 mm and four extensions rings (two of 27.5 mm, one of 25 mm and the other one of 14 mm) situated at 118 mm from the droplets. The droplets were generated by vibrating a jet of 400  $\mu\text{m}$  at a frequency of 6.73KHz thus providing a stream of monodisperse droplets of 675  $\mu\text{m}$ . The model used was the DBK003, which has a chord of 690 mm, moving at 90 m/s. An ampliation of the portion of the image recorded is shown in Figure 16. It can be observed that the resultants droplets are not blurred as before, however the background is not uniform which hinder the measurements.

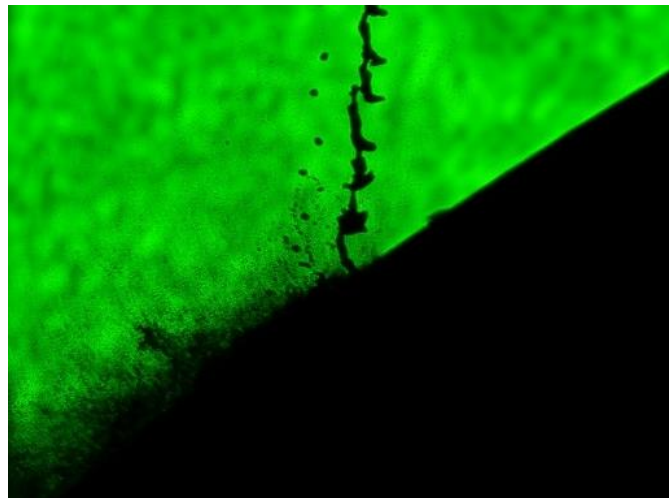


Figure 16: Droplets of 675  $\mu\text{m}$  approached by the DBK003 airfoil model moving at 90 m/s.

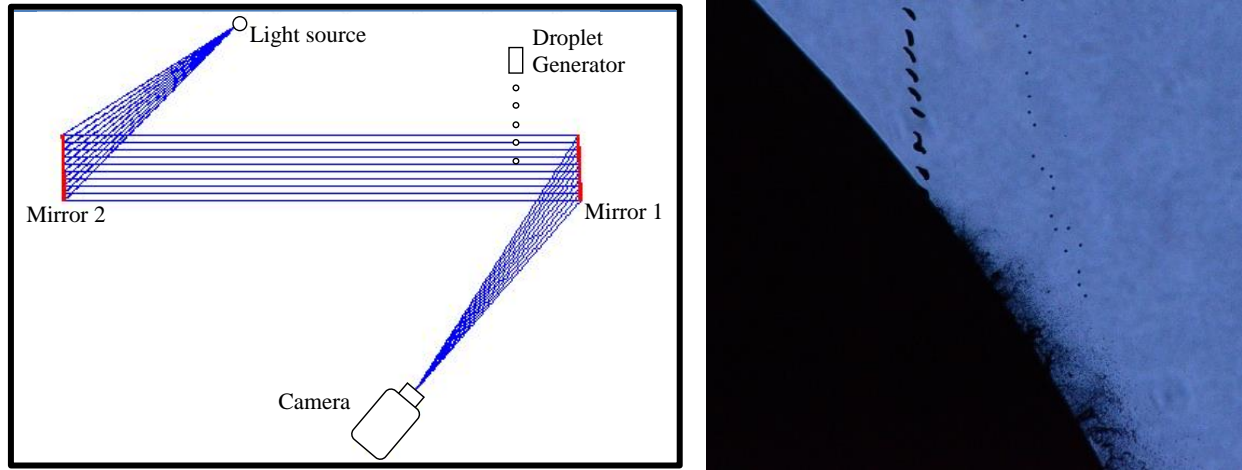


Figure 17: Experimental setup of the acquisition system (left) example of image using nanoflash illumination (right)

Finally, the nanoflash was used to illuminate from the back using the parabolic mirror while the camera recorded images from another parabolic mirror. The configuration is shown in Figure 17 left and an amplification of the portion of the image obtained while the model was moving at 70 m/s is shown in Figure 17 right. It can be observed that now the background allows the measurements and the resultant droplets are sharp. Therefore, this technique seems to be the more adequate for measuring the resultant droplets. However, future investigation should be done regarding the way of analysing these images.

## 8.2 Supercooled Large Droplets (SLD)

Up to now, only droplets at ambient temperature have been tested. However, if it was possible to generate supercooled large droplets in a controlled manner, they could also be tested in the facility. The first challenge is to control the generation of the droplets. The second challenge is to measure the temperature of the droplets during the test since the droplet will be heated while they are falling (the facility is at ambient temperature). On one hand, it is necessary a non-intrusive technique to measure the temperature. Otherwise, the airfoil model would intercept the sensor. On the other hand, a rapid response is mandatory since the time between two passes of the model is very short, on the order of 0.15s. Infrared cameras works receiving the signal emitted by the droplet, which increase with the temperature. Therefore, for droplet supercooled, with low temperature, the response time to measure the temperature would increase preventing the use for this application. Other techniques such as the spectrometry of Raman [22] should be employed.

A theoretical study has been performed to evaluate the increase in temperature of the falling droplets. To do so, the droplet is assumed to be a perfect sphere in free fall subjected to the flow field generated by the model approach. Firstly, the free fall dynamics problem is solved. The results of that problem are later used for solving the transient heat transfer equation given by

$$\rho_d c_p V \frac{dT}{dt} = -S(h_c(T - T_\infty) + h_d \rho_{amb} \Delta H_{vap}(w_s - w_\infty)) \quad (6)$$

where  $\rho_d$  is the droplet density,  $c_p$  is the specific heat of water,  $V$  is the droplet volume,  $T$  is the droplet temperature,  $S$  is the droplet surface,  $h_c$  is the forced convection coefficient,  $T_\infty$  is the ambient temperature,  $h_d$  is the mass convection coefficient,  $\rho_{amb}$  is the ambient density,  $\Delta H_{vap}$  is the enthalpy of vaporization,  $w_s$  is the droplet surface humidity ratio at  $T$  and  $w_\infty$  is the ambient humidity ratio.

Figure 18 shows the evolution of the temperature versus the distance to the stagnation line for different droplets diameters. It can be observed that the temperature increase can be up to 15° for droplets of 400  $\mu\text{m}$  while is only 0.3° for droplets of 2 mm. Therefore, smaller droplets must be supercooled greater to take into account this effect.

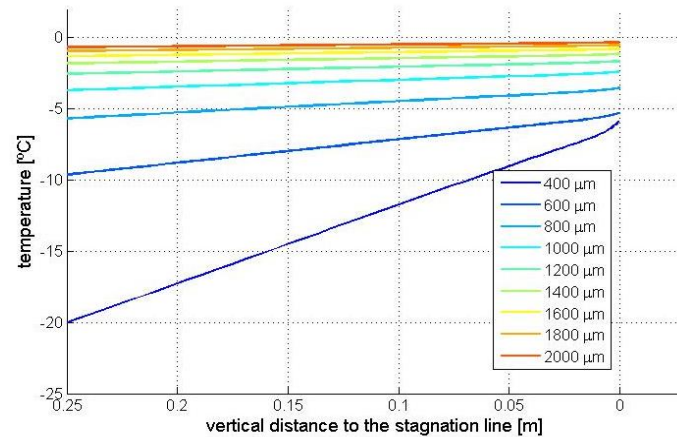


Figure 18: Heating of supercooled droplets during the fall

## 8. Conclusions

The rotating rig facility consists of an arm of 2 m length moved by a motor of 5kW of power with a vertical axis. The maximum rotational velocity is 400 rpm. At the end of the arm, the airfoil tested is mounted reaching velocities up to 90 m/s. Droplets are generated and allowed to fall in the path of the airfoil while the recording system (either high speed camera or high resolution camera) is working. Different illumination techniques, either direct or shadowgraph are employed. A new set of airfoils models have been built and characterised by means of LDV experiments providing the installation with new velocities profiles in the test section. A study of the influence of the airfoil wake in the test section has been performed by means of LDV experiments showing that the main influence is a residual velocity at one chord of the leading edge that ranged between 2% to 4% depending on the model. PIV tests were performed to study the two-dimensionality assumption in the test region. It was found that, though slightly asymmetry is observed due to the arm rotation, there is a region in the centre of the spanwise direction of width 2 cm where this assumption is valid being the error on the order of 2%.

A comparison of the rotating rig facility to the wind tunnel facility has been performed in terms of the flow field, the operational cost and the droplet location, leading to the following conclusions:

- The droplets in the rotating rig facility suffer acceleration while in the wind tunnel facility would suffer deceleration.
- The operational cost was found to be 1000 times less in the rotating rig and the field of view necessary 35 times smaller.
- The droplet location is also easier in the rotating rig facility than in wind tunnel.

Also, as a result of the experiments conducted in the rotating rig facility, some new models of droplets deformation, trajectory and breakup have been developed taking into account the continuously accelerated flow field, thus showing the benefits to the previous models. Droplets deformation and breakup phenomenon are strongly dependent on the droplet size, the leading-edge radius of the airfoil tested and its velocity. Summarizing, it can be concluded that the rotating rig facility is better than the wind tunnel for studying droplets in the vicinity of airfoils in terms of flow field, cost of operation or droplet location, which is confirmed with the benefits of the models developed thanks to this facility.

Finally, preliminary studies on future applications such as the splashing phenomenon or tests with supercooled large droplets have been also performed. First of all, it has been evidenced that there is an influence of the breakup in the splashing phenomenon and different techniques of illumination have been tested. The strobotac 1538-A microflash was used both, as direct and as shadowgraph illumination, and it was found that the duration is not short enough to capture the resultant droplets that depart from the surface. A laser was also used for illumination, however, though now the duration was short enough, the background of the images hindered the measurements. Finally, the NANOLITER flash was used to illuminate from the back using a parabolic mirror while the camera recorded images from another parabolic mirror. It was found that this technique seems to be the more adequate for measuring the resultants droplets. However, future investigation should be done regarding the way of analysing these images. Finally, regarding the generation of supercooled large droplets, it can be concluded that it is necessary to supercool them less than smaller droplets.

## Acknowledgements

This investigation has been funded by the Ministry de Economy, Industry and Competitiveness of Spain (MINECO), as part of the project DFLOW DPI2016-75296-P. This has also been funded by the by INTA, under the project “Termofluidodinámica”.

## References

- [1] Cao Y, Wenyuan T. and Zhenlong W. 2018. Aircraft icing: An ongoing threat to aviation safety. *Aerospace Science and Technology*. 75: 353-385.
- [2] Jiaqi W, Zhenlong W. and Yan S. 2018. Aircraft icing safety analysis method in presence of fuzzy inputs and fuzzy state. *Aerospace Science and Technology*. 82-83: 172-184.
- [3] Zhenlong W., Benyin L. and Yiahua C. 2018. Heavy rain effects on aircraft lateral/directional stability and control determined from numerical simulation data. *Aerospace Science and Technology*. 80: 472-481
- [4] Zhenlong W. and Yiahua C. 2016. Airfoil performance degradation by coupling effects of supercooled raindrop icing and heavy rain fall. *J. Aerospace Engineering*. 231: 2384-2395.
- [5] García-Magariño A., Sor S. and Velazquez A. 2015. Experimental characterization of water droplet breakup in the vicinity of a moving airfoil. *Aerospace Science and Technology*. 45: 490-500
- [6] Vargas M., Sor S. and García-Magariño A. 2012. Mechanism of water droplet breakup near the leading edge of an airfoil. In : *4th AIAA atmospheric and space environments conference*.
- [7] García-Magariño A., Sor S. and Velazquez A. 2017. Droplet breakup criterion in airfoils leading edge vicinity. In: *9th AIAA Atmospheric and Space Environments Conference*.
- [8] Guildenbecher D., Lopez-Rivera C. and Sojka P. 2009. Secondary atomization. *Experiments in fluids*. 46: 371-402
- [9] Theofanous T. 2011. Aerobreakup of newtonian and viscoelastic fluids. *Annual review of fluid mechanics*. 43: 661-690
- [10] Suryaprakash R. and Tomar G. 2019. Secondary breakup of drops. *J. Indian Ins. Sci*. 99 :77-91
- [11] Wright W. 2008. User’s Manual for LEWICE Version 3.2. Agard Advisory Report 345. NASA/CR-2008-214255
- [12] Temkin S. and Mehta H. 1982. Droplet drag in an accelerating and decelerating flow. *Journal of Fluid Mechanics*. 116: 297-313
- [13] Feo A., Vargas M. and Sor S. 2011. Rotating rig development for droplet deformation/breakup and impact induced by aerodynamic surfaces. *SAE International*.
- [14] Barlow J., Rae W. and Pope A. Low-speed wind tunnel testing. *John Wiley & Son, 1999*
- [15] García-Magariño A., Sor S. and Velazquez A. 2016. Model to predict water droplet trajectories in the flow past an airfoil.
- [16] Sor S. and García-Magariño A. 2015. Modeling of droplet deformation near the leading edge of an airfoil. *Journal of Aircraft*. 52 No.6
- [17] Ibrahim E., Yang H. and Przekwas A. 1993. Modeling of spray droplets deformations and breakup. *Journal of Propulsion and Power*. 9: 651-654
- [18] Clark M. 1988. Drop breakup in a turbulent flow- I, conceptual and modelling considerations. *Chemical Engineering Science*. 43: 671-679
- [19] García-Magariño A., Sor S. and Velazquez A. 2019. Droplet in the Shoulder Region of an Incoming Airfoil. Part I: Droplet Deformation and Trajectory. *American Institute of Aeronautics and Astronautics*. (to be published)
- [20] García-Magariño A., Sor S. and Velazquez A. 2019. Droplet in the Shoulder Region of an Incoming Airfoil. Part II: Droplet Breakup. *American Institute of Aeronautics and Astronautics*. (to be published)
- [21] Pilch M., Erdman C. 1987. Use of breakup time data and velocity history data to predict the maximum size of stable fragments for acceleration-induced breakup of liquid drop. *International Journal of Multiphase Flow*. 13: 741-757.
- [22] Goy C., Potenza M., Dederá S., Tomut M., Guillerm E., Kalinin A., Voss K., Schottelius A., Pedridis N., Prosvetov A., Tejada G., Fernández J.M., Trautmann C., Caupin F., Glasmacher U. and Grisenti R. 2018. Shrinking of Rapidly Evaporating Water Microdroplets Reveals their Extreme Supercooling. *Physical Review Letter*. 120.1: 015501